On the Use of Standing Oblique Detonation Waves in a Shcramjet Combustor[1]

Giovanni Fusina
Defence R & D Canada, Ottawa, Canada
501-1025 Grenon Ave. Ottawa, Ontario, K2B-8S5, Canada
giovanni.fusina@utoronto.ca

Jean P. Sislian
University of Toronto Institute for Aerospace Studies, Toronto, Canada

Alexander O. Schwientek
Stuttgart University, Stuttgart, Germany

Bernard Parent
Department of Aerospace Engineering, Seoul National University, Seoul, South Korea

Keywords: Shcramjet, Combustor, Oblique Detonation Wave

Abstract

The *sh*ock-induced *c*ombustion *ramjet* (shcramjet) is a hypersonic airbreathing propulsion concept which overcomes the drawbacks of the long, massive combustors present in the scramjet by using a standing oblique detonation wave (a coupled shock-combustion front) as a means of nearly instantaneous heat addition. A novel shcramjet combustor design that makes use of wedge-shaped flameholders to avoid detonation wave-wall interactions is proposed and analyzed with *c*omputational *f*luid *d*ynamics (CFD) simulations in this study. The laminar, two-dimensional Navier-Stokes equations coupled with a non-equilibrium hydrogen-air combustion model based on chemical kinetics are used to represent the physical system. The equations are solved with the WARP (*w*indow-*a*llocatable *r*esolver for *p*ropulsion) CFD code (see: Parent, B. and Sislian, J. P., "The Use of Domain Decomposition in Accelerating the Convergence of Quasihyperbolic Systems", J. of Comp. Physics, Vol. 179, No. 1, 2002, pages 140–169). The solver was validated with experimental results found in the literature. A series of steady-state numerical simulations was conducted using WARP and it was determined by means of thrust potential calculations that this combustor design is a viable one for shcramjet propulsion: assuming a shcramjet flight Mach number of twelve at an altitude of 36,000 *m*, the geometrical dimensions used for the combustor give rise to an operational range for combustor inlet Mach numbers between six and eight. Different shcramjet flight Mach numbers would require different combustor dimensions and hence a variable geometry system in order to be viable.

Introduction

All space launches from Sputnik in 1957 to date have used multistaged rocket propulsion as a means of achieving Earth orbit. This method, although successful, is rather inefficient since approximately two-thirds of the vehicle's takeoff mass is taken up by the oxidizer while less than one-twentieth of the takeoff mass is reserved for the payload [1]. It is clear that augmenting the rocket engine with an airbreathing propulsion system capable of accelerating the space vehicle to very high Mach numbers (approximately 20) and very high altitudes (approximately 50 *km*) would entail greater efficiency and cost effectiveness because the amount of on-board oxidant could be drastically reduced and replaced with payload mass. Rocket engines would still need to be used in the latter stages of the orbital flight at altitudes where the air density is too low for an airbreathing engine to function.

A turboramjet (a combination of a turbojet and a ramjet) could be used for the low flight Mach number range (0–6). Ramjets become drastically inefficient at flight Mach numbers greater than six since the deceleration of such a high speed flow to subsonic speeds in the combustor occurs with high losses in stagnation pressure and causes the combustor entrance temperature to be high enough to cause dissociation of nitrogen and oxygen, leading to decreased combustion efficiency. For flight Mach numbers higher than six, therefore, supersonic combustion must be employed.

For this reason, the hypersonic airbreathing propulsion research community has devoted much effort in recent years in the study of the scramjet (*s*upersonic *c*ombustion *ramjet*) [2]: a diffusive burning engine where the oncoming airstream is first decelerated in a diffuser by a series of oblique shocks to supersonic velocities (on the order of several thousand meters per second), raising its temperature and pressure; fuel is then injected in the combustor and diffusive mixing and burning occur simultaneously at supersonic speeds;

finally, the combustion products are expanded through a nozzle to provide thrust.

The most vigorous and recognizable effort in scramjet research and development and even prototype construction is the United States National Aeronautics and Space Administration's Hyper-X program [2]. Other examples of past and present research efforts for the scramjet concept include the *N*ational *A*ero*S*pace *P*lane (NASP) program also in the United States [1], the "*Pro*gramme de *RE*cherche et de technologie sur la *P*ropulsion *H*ypersonique *A*vancée" (PREPHA) program in France [3] and the National Aerospace Lab Spaceplane program in Japan [4].

The scramjet is a promising concept, but its performance is hampered due to its diffusive burning characteristics. To avoid losses due to interactions between the injected fuel and the airstream, the fuel must be injected parallel to the airstream. The parallel fuel injection causes slow mixing, and therefore, a long combustion chamber is required to achieve an adequate heat release from the combustion. The scramjet is therefore said to be mixing-limited, *i.e.*, the rate of mixing and burning is limited by the rate of diffusion of fuel into the airstream [5]. This leads to a larger overall engine structure and a more complex cooling system, which increases the weight and degrades the efficiency of such an engine. At higher Mach numbers, the mixing layer growth is reduced, requiring an even longer and more massive combustor. An engine requiring a much smaller combustion chamber would therefore greatly benefit the hypersonic airbreathing propulsion effort.

The *sh*ock-induced *c*ombustion *ramjet* (shcramjet) [6, 7] is an alternate mode of hypersonic airbreathing propulsion that eliminates the need for the long and massive scramjet combustion chamber by utilizing a thin oblique detonation wave to burn a *premixed* supersonic fuel-air mixture. The use of the detonation wave has prompted some researchers to refer to the shcramjet as the oblique detonation wave ramjet, or, oblique detonation wave engine [8].

Shown in Figure 1 is an idealized schematic of an external compression shcramjet engine. The fuel injection takes place in the inlet near the leading edge of the engine, taking advantage of the long inlets typical of hypersonic airbreathing engines. The inlet also decelerates the flow by means of two equal-strength oblique shock waves in order to minimize losses (see Oswatitsch [9]). Since both shocks occur outside the cowl and body flow, the compression is external, hence the expression "external compression shcramjet". The shcramjet inlet is designed such that the temperature and pressure of the fuel-air mixture at its exit is just below the ignition point of the fuel. A third shock, emanating from the cowl, raises the pressure and temperature past this ignition point and, after an induction distance, the fuel starts to burn: the ensuing combustion front couples with the third shock, forming an oblique detonation wave. Since only the fuel-air reactions determine the rate of the combustion and the length of the combustor, the shcramjet is said to be rate-limited [5], *i.e.* chemical reaction rate-limited. The combustion products are then expanded through a nozzle to provide thrust. Hydrogen is usually considered the fuel

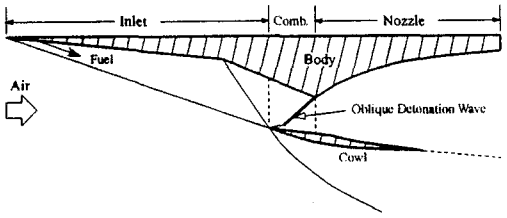

Fig. 1: External compression shcramjet configuration.

of choice for shcramjet (and scramjet) propulsion. This is because of its very high heating value compared to hydrocarbon fuels and because the cryogenic storage temperatures would help in providing the necessary surface cooling to the vehicle [5].

The idea of using standing detonation waves for hypersonic propulsion dates to 1946 and is attributed to Roy [10]. Preliminary one-dimensional studies by Dunlap *et al.* [11] and Sargeant and Gross [12] in the late 1950s were followed by more detailed analytical models by Townend [13], Morrison [14, 15], Ostrander *et al.* [16], O'Brien *et al.* [17], Menees *et al.* [18] and Sheng and Sislian [19] in the 1970s and 1980s. Inviscid simulations using *c*omputational *f*luid *d*ynamics (CFD) methods of entire shcramjet flowfields were carried out by Dudebout and Sislian [20, 5] in the 1990s and their findings confirmed the results of the analytical work of the previous decades: first, the shcramjet has a superior performance to the scramjet for high flight Mach numbers, and second, the shcramjet shows a fuel specific impulse greater than that of a rocket for flight Mach numbers below twenty-two. Further studies by Sislian *et al.* [21, 22] comparing on and off design shcramjet performance between mixed compression (where the compression takes place both internal and external to the engine duct) and external compression systems concluded that the mixed compression system results in a higher fuel specific impulse in both on design and off design cases.

One inherent technical challenge to shcramjet propulsion is to realize adequate mixing of fuel and air before the start of the combustor while preventing premature ignition. The effects of incomplete mixing were studied by Schumacher and Sislian [23, 21] and it was shown that a varying equivalence ratio distribution decreased the fuel specific impulse by as much as 40% between flight Mach numbers of 9 and 24. Studies in fuel injection strategies in the inlet were undertaken by Schumacher, Parent and Sislian [24, 25], which showed that cantilevered fuel injectors that make use of baroclinic torque offer a viable fuel-injection system. More studies are presently being conducted to determine the

best strategy for preventing premature ignition.

A fundamental question critical to the success of shcramjet propulsion is the assumed ability to stabilize a detonation wave in the combustor section. Some preliminary studies on the detonation wave's stability to inhomogeneities in the oncoming fuel-air flow due to incomplete mixing have been carried out [26, 27], but more investigation must follow in this area.

Further, the studies that calculated shcramjet performance all assumed inviscid flow and therefore did not consider the possible viscous effects of detonation wave-wall interactions. The combustor design used in these studies is therefore relatively simple: it consists of a single oblique detonation wave attached to the cowl of the engine. No combustor design strategy has been developed to avoid the massive recirculation zone that would form when the detonation wave impinges on the shcramjet's body surface. This present study will attempt to address the above stated issue.

Oblique Detonation Wave Behaviour

A shock in a supersonic or hypersonic flow of a combustible mixture can raise the temperature and pressure of the mixture to values high enough to induce combustion. In this combustion process, a short ignition delay – where temperature and pressure remain nearly constant but the concentration of radical species increases by orders of magnitude – is followed by an exothermic process were the production of combustion products take place. If the heat release occurs sufficiently close to the shock, such that a coupled shock-flame front is formed, this structure is termed a detonation wave [28, 5].

Detonation waves can either propagate in a combustible mixture or be standing in a hypersonic flow of a combustible mixture over a wedge or blunt body. Propagating detonation waves can have multi-dimensional structures which are inherently unsteady and are made up of complex interactions between the leading shock and the reaction front. This phenomenon is termed "cellular structure of detonation waves" [29, 30]. This phenomenon has been studied at length in the past (see for example [29, 31, 32]) and is beyond the scope of this present study.

For the case of a blunt-body shaped projectile travelling at hypersonic speeds in a hydrogen-air mixture, both steady and unsteady detonation wave structures have been observed experimentally [33] and modelled at length computationally [34, 35, 36].

The typical structure of an oblique detonation wave stabilized over a wedge is shown in Figure 2. This structure was studied and described in detail by Li *et al.* [30] by means of numerical simulations and observed experimentally by Viguier *et al.* [37]. A shock formed by a wedge (which deflects the flow by an angle δ) increases the temperature of the oncoming fuel-air mixture above the ignition point of the fuel. This shock is termed the combustion-inducing shock. In the induction region – the region between the combustion-inducing shock and the first deflagration wave – concentration of radicals increase (with temperature and pressure remaining almost constant) until an exothermic process begins, with the concentration of water and other combustion products increasing exponentially, and with deflagration waves being formed. These propagate upward at the local Mach angle. Each successive deflagration wave has a steeper angle than the former due to the temperature rise across each successive wave [30]. The deflagration waves at first merge into each other, until they all merge into the combustion-inducing shock. The shock and deflagration waves become coupled into a single wave-front which is termed an *o*blique *d*etonation *w*ave (ODW). The ODW angle (ε) is much steeper than the combustion-inducing shock angle. A slip line (contact surface) is also formed separating the component of flow passing through the ODW and the component of flow passing through the shock and the deflagration waves. This latter component is also termed the "shock-induced combustion zone". A

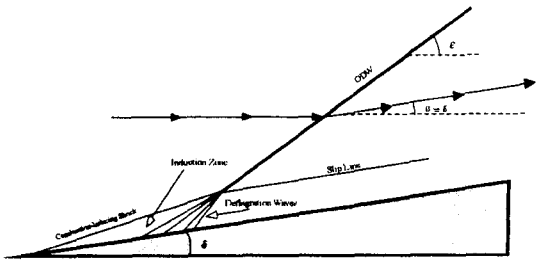

Fig. 2: Schematic of an ODW (θ is the flow angle).

limiting condition for detonation waves is the Chapman-Jouguet (CJ) point of minimum entropy where the Mach number of the combustion products downstream of the wave is unity: this implies a self-sustaining detonation. For the case of *oblique* detonation waves, the CJ condition corresponds to a particular wedge angle –δ_{CJ}– which gives rise to a CJ-ODW at an angle ε_{CJ}: the downstream Mach number in the flow component normal to the ODW is unity. It has been observed, in a series of both inviscid [5] and viscous [26] numerical simulations, that lowering the wedge angle below δ_{CJ} does not entail a lower ODW angle than ε_{CJ}: this re-enforces the notion of a self-sustaining detonation at CJ. Since the CJ point also corresponds to minimum entropy production, the shcramjet is usually designed to operate with an ODW close to CJ conditions. [20]

Scope of this Study

A novel shcramjet combustor design is proposed herein in order to eliminate the detonation wave-wall interaction that would be present in previous shcramjet combustor designs. Figure 1 shows the original shcramjet configuration used by Dudebout [5] for his preliminary

study of shcramjet performance. Its combustor utilizes a single oblique detonation wave in the combustor with the cowl, in essence, acting as one large flame-holder for the ODW. This approach would lead to the formation of an undesirably large recirculation zone as the ODW would impinge onto the body surface just before the beginning of the nozzle section. This recirculation region could adversely affect the performance of the shcramjet by considerably increasing drag and lowering the overall thrust potential of the combustor. The new design (shown in Figure 4 together with the original shcramjet combustor design) proposed here utilizes wedge-shaped flame-holders configured in such a manner as to prevent ODW-wall interactions.

A second advantage of the new design is realized by considering off-design conditions. Inviscid simulations by Islam [38] based on the original shcramjet combustor design have shown that off-design conditions severely affect shcramjet performance: particularly in the combustor, off-design conditions would cause the ODW angle to change, giving rise to a reflected shock, and the resulting recirculation zone from this interaction could be even larger than one resulting from on-design conditions. Furthermore, this reflected shock would cause the temperature to increase to values high enough to incur into significant dissociation which would decrease the heat released and the thrust potential of such a combustor. The novel configuration would reduce these undesirable effects, since the ODWs would change position upstream or downstream but would not interact with the wall. Note in

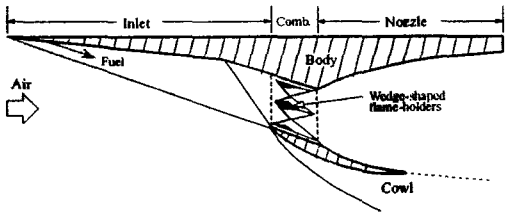

Fig. 3: Alternate external compression shcramjet configuration.

Figure 4, the gap placed between the flame holders and the body surface or the cowl surface. This is to prevent the interaction of the boundary layer on the cowl or on the body surface to interact with the formation region of the ODWs. Such an interaction could also lead to recirculation zones and a corresponding loss of thrust potential.

The scope of this study does not include an analysis of the effects of the body-surface wall, or of the cowl-surface wall on this combustor design. Only one-quarter of the entire combustor flowfield (*i.e.* a height of D/2 in Figure 4) is solved with numerical steady-state simulations, and is analyzed to determine its thrust potential and heat released, as well as the skin friction drag of the wedge-shaped flameholders. This study proceeds by first giving a description of the problem setup, followed by an explanation of the calculation of thrust potential and drag. The accuracy of the computational grid used is assessed by a grid convergence study, and the results of the numerical simulations are finally presented and analyzed.

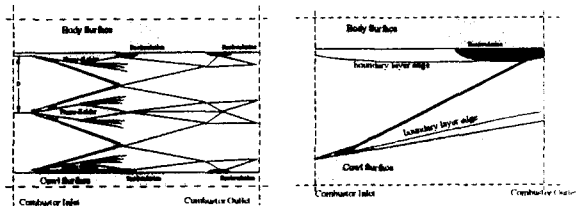

Fig. 4: **Left:** schematic of shcramjet combustor using diamond-shaped flame-holders. *Right:* original shcramjet combustor configuration.

Physical Model and Numerical Method

The laminar, two-dimensional, multi-species Navier-Stokes equations are used herein to model the physical system. They are written below in tensor form in curvilinear co-ordinates [39, 40, 41] as:

$$\frac{\partial}{\partial t}Q+\sum_{i=1}^{n_d}\left[\frac{\partial F_i}{\partial X_i}-\sum_{j=1}^{n_d}\frac{\partial}{\partial X_i}\left(K_{i,j}\frac{\partial G}{\partial X_j}\right)\right]=S \qquad (1)$$

where the vector of conservative variables, Q, convection fluxes, F_i, diffusion fluxes, G, and source terms, S can each be written as [41]:

$$Q=\frac{1}{J}\begin{bmatrix}\rho c_1\\ \vdots\\ \rho c_{n_s}\\ \rho v_1\\ \vdots\\ \rho v_{n_d}\\ \rho E\end{bmatrix},\quad F_i=\frac{1}{J}\begin{bmatrix}\rho V_i c_1\\ \vdots\\ \rho V_i c_{n_s}\\ \rho V_i v_1+X_{i,1}P\\ \vdots\\ \rho V_i v_{n_d}+X_{i,n_d}P\\ \rho V_i E+V_i P\end{bmatrix},\quad G=\begin{bmatrix}c_1\\ \vdots\\ c_{n_s}\\ v_1\\ \vdots\\ v_{n_d}\\ T\end{bmatrix},\quad S=\frac{1}{J}\begin{bmatrix}W_1\\ \vdots\\ W_{n_s}\\ 0\\ \vdots\\ 0\\ 0\end{bmatrix}. \qquad (2)$$

The rate of change of the distance in the curvilinear coordinate system with respect to the Cartesian coordinate system, $X_{i,j}$, is given by:

$$X_{i,j}=J\left[\left(2\delta_{i,j}^{K}-1\right)\frac{\partial x_{j+1}}{\partial X_{i+1}}\right] \qquad (3)$$

in two dimensions. The inverse of the metric Jacobian, $1/J$, also in two dimensions, corresponds to:

$$\frac{1}{J}=\frac{\partial x_1}{\partial X_1}\frac{\partial x_2}{\partial X_2}-\frac{\partial x_1}{\partial X_2}\frac{\partial x_2}{\partial X_1}. \qquad (4)$$

The contravariant velocity V_i has the usual definition:

$$V_i\equiv\sum_{j=1}^{n_d}X_{i,j}v_j. \qquad (5)$$

The diffusion matrix $K_{i,j}$ is given by [41]:

$$K_{i,j} = \begin{bmatrix} \alpha_{i,j}v_1 & \cdots & 0 & 0 & \cdots & 0 & 0 \\ \vdots & \ddots & \vdots & \vdots & \ddots & \vdots & \vdots \\ 0 & \cdots & \alpha_{i,j}v_{n_d} & 0 & \cdots & 0 & 0 \\ 0 & \cdots & 0 & \mu\beta_{i,j}^{1,1} & \cdots & \mu\beta_{i,j}^{1,n_d} & 0 \\ \vdots & \ddots & \vdots & \vdots & \ddots & \vdots & \vdots \\ 0 & \cdots & 0 & \mu\beta_{i,j}^{n_d,1} & \cdots & \mu\beta_{i,j}^{n_d,n_d} & 0 \\ \alpha_{i,j}h_1v_1 & \cdots & \alpha_{i,j}h_{n_d}v_{n_d} & \mu\sum_m v_m\beta_{i,j}^{m,1} & \cdots & \mu\sum_m v_m\beta_{i,j}^{m,n_d} & \alpha_{i,j}\kappa \end{bmatrix} \tag{6}$$

where α and β correspond to

$$\alpha_{i,j} = \frac{1}{J}\sum_{m=1}^{n_d} X_{j,m}X_{i,m}\,, \quad \beta_{i,j}^{mn} = \alpha_{i,j}\delta_{mn}^{K} + \frac{1}{J}X_{j,m}X_{i,n} - \frac{2}{3}\frac{1}{J}X_{j,n}X_{i,m}\,. \tag{7}$$

Note that v_i is the velocity component of the mixture in the x_i direction; c_k is the mass fraction of species k; h_k is the enthalpy of species k; T, P and ρ are the mixture temperature, pressure and density respectively; δ_{ij}^{K} is the Kronecker delta; n_d is the number of dimensions; and n_s is the number of species. The total energy of the mixture, E, is given by:

$$E = e + \sum_{j=1}^{n_d}\frac{v_j^2}{2}\,. \tag{8}$$

The Navier-Stokes equations are closed by the thermal and caloric equations of state:

$$P = \sum_{k=1}^{n_s}\rho c_k R_k T \tag{9}$$

$$e = \sum_{k=1}^{n_s} c_k h_k - \frac{P}{\rho} \tag{10}$$

where R_k is the gas constant for species k and the species enthalpies are calculated from:

$$h_k = R_k\left(a_{1,k}T + \frac{a_{2,k}}{2}T^2 + \frac{a_{3,k}}{3}T^3 + \frac{a_{4,k}}{4}T^4 + \frac{a_{5,k}}{5}T^5 + a_{6,k}\right) \tag{11}$$

where the coefficients $a_{1,k}$ to $a_{6,k}$ are part of McBride's polynomial formulation [42] of the thermochemical data found in the JANAF tables [43]. These polynomials can also be used to calculate the species specific heats at constant pressure, C_{Pk}:

$$C_{Pk} = R_k\left(a_{1,k} + a_{2,k}T + a_{3,k}T^2 + a_{4,k}T^3 + a_{5,k}T^4\right)\,. \tag{12}$$

The McBride polynomials are valid from a temperature of 200 K to one of 6000 K.

The mixture viscosity μ, mixture thermal conductivity κ and species mass diffusion coefficient ν_k are determined from the kinetic theory of gases (see Dixon-Lewis [44] for a derivation of the needed expressions), while the rates of species production due to non-equilibrium chemical reactions, $\dot{W}_k$, are determined from Arrhenius chemical kinetics [45]. Each species production term is given by:

$$\dot{W}_k = m_k\sum_{l=1}^{N_e}\left(v_{l,k}'' - v_{l,k}'\right)\left[k_{f,l}\prod_{m=1}^{N_l}[\chi_m]^{v_{l,m}'} - k_{b,l}\prod_{m=1}^{N_l}[\chi_m]^{v_{l,m}''}\right] \tag{13}$$

where N_e is the number of elementary reactions involving species k, N_l is the number of species involved in the elementary reaction, m_k is the molecular weight of species k, χ_m is the mole fraction of species m, $v_{l,k}'$ is the stoichiometric coefficient for the reactants of reaction l, $v_{l,k}''$ is the stoichiometric coefficient for the products of reaction l, k_b is the backward reaction rate constant and k_f is the forward reaction rate constant, given by the modified Arrhenius equation:

$$k_f = \mathscr{A}T^n\exp(-\mathscr{E}/\mathscr{R}T)\,. \tag{14}$$

The coefficients $\mathscr{A}$, n and $\mathscr{E}$ for each elementary reaction are tabulated in so-called "combustion models". Here, the Jachimowski [46] model was used for hydrogenair combustion: it uses twenty reactions and nine species with nitrogen inert and it is shown in Table 1. The backward and the forward reaction rate constants are related by the equilibrium constant, K_c:

$$K_c = \frac{k_f}{k_b}\,. \tag{15}$$

The equilibrium constant, K_c is given by:

$$K_c = (\mathscr{R}T)^{-\Delta\nu}\exp\left(\frac{-\Delta G^0}{\mathscr{R}T}\right) \tag{16}$$

where

$$\Delta\nu = \sum_{i=1}^{N_l}(v_i'' - v_i') \tag{17}$$

and ΔG^o is the difference in Gibbs free energy between products and reactants in a particular reaction, calculated at a reference pressure of 1 atm, given by:

$$\Delta G^o = \sum_{k=1}^{N_l}(v_k'' - v_k')\,(h_k - Ts_k^o) \tag{18}$$

where h_k is the molar enthalpy of the species k, and s_k^o is the molar entropy of species k calculated at a reference pressure of one atmosphere. Finally, note that in Table 1, the symbol M denotes a third-body collision partner, a species acting as a catalyst only. The molar concentration of M is simply determined from the equation:

$$\chi_M = \sum_{k=1}^{n_s}\eta_k\chi_k \tag{19}$$

where η_k is the third-body efficiency. η_k is unity for most species and reactions except those listed in Table 2.

The computational results were obtained with the *w*indow *a*llocatable *r*esolver for *p*ropulsion (WARP) CFD code [47, 41] developed by Parent at the University of Toronto Institute for Aerospace Studies. It was used to solve the the system of equations described above. WARP employs the Roe scheme [48] – turned second-order accurate by a TVD minmod limiter by Yee [49] – for convective flux discretization, central

Table 1: Jachimowski combustion model equations and parameters.

	Reaction	α	n	β
(1)	$H_2+O_2 \rightleftharpoons OH+OH$	1.70×10^{13}	0	48 000
(2)	$H+O_2 \rightleftharpoons OH+O$	2.60×10^{14}	0	16 800
(3)	$O+H_2 \rightleftharpoons OH+H$	1.80×10^{10}	1.00	8 900
(4)	$OH+H_2 \rightleftharpoons H_2O+H$	2.20×10^{13}	0	5 150
(5)	$OH+OH \rightleftharpoons H_2O+O$	6.30×10^{12}	0	1 090
(6)	$H+OH+M \rightleftharpoons H_2O+M$	2.20×10^{22}	-2.00	0
(7)	$H+H+M \rightleftharpoons H_2+M$	6.40×10^{17}	-1.00	0
(8)	$H+O+M \rightleftharpoons OH+M$	6.00×10^{16}	-0.60	0
(9)	$H+O_2+M \rightleftharpoons HO_2+M$	2.10×10^{15}	0	-1 000
(10)	$HO_2+H \rightleftharpoons H_2+O_2$	1.30×10^{13}	0	0
(11)	$HO_2+H \rightleftharpoons OH+OH$	1.40×10^{14}	0	1 080
(12)	$HO_2+H \rightleftharpoons H_2O+O$	1.00×10^{13}	0	1 080
(13)	$HO_2+O \rightleftharpoons O_2+OH$	1.50×10^{13}	0	950
(14)	$HO_2+OH \rightleftharpoons H_2O+O_2$	8.00×10^{12}	0	0
(15)	$HO_2+HO_2 \rightleftharpoons H_2O_2+O_2$	2.00×10^{12}	0	0
(16)	$H+H_2O_2 \rightleftharpoons H_2+HO_2$	1.40×10^{12}	0	3 600
(17)	$O+H_2O_2 \rightleftharpoons OH+HO_2$	1.40×10^{13}	0	6 400
(18)	$OH+H_2O_2 \rightleftharpoons H_2O+HO_2$	6.10×10^{12}	0	1 430
(19)	$M+H_2O_2 \rightleftharpoons OH+OH+M$	1.20×10^{17}	0	45 500
(20)	$O+O+M \rightleftharpoons O_2+M$	6.00×10^{17}	0	-1 800

The units for α are in $[\frac{cm^{3b}}{(gmol-s)^b}]$ where $b = 1$ for two body reactions and $b = 2$ for three body reactions. β is in $[\frac{cal}{gmol}]$.

Table 2: Third body efficiencies for Jachimowski model.

	Reaction	third body efficiency			
(6)	$H+OH+M \rightleftharpoons H_2O+M$	H_2	1.0	H_2O	6.0
(7)	$H+H+M \rightleftharpoons H_2+M$	H_2	2.0	H_2O	6.0
(8)	$H+O+M \rightleftharpoons OH+M$	H_2	1.0	H_2O	5.0
(9)	$H+O_2+M \rightleftharpoons HO_2+M$	H_2	2.0	H_2O	16.0
(19)	$M+H_2O_2 \rightleftharpoons OH+OH+M$	H_2	1.0	H_2O	15.0

differences for diffusive flux discretization, and a block-implicit approximate factorization algorithm to advance the solution in pseudo-time. Time accuracy may be regained by a dual-time stepping method [50]. To achieve faster convergence, WARP uses a domain decomposition technique termed the "marching window cycle" which is explained in detail in Ref. [47]: it is important to note that it does not modify the discretized residual, the block-implicit factorization scheme, the dual time stepping scheme, nor the convergence criterion [41].

In WARP, the residual of the laminar Navier-Stokes equations is defined in tensor form in curvilinear coordinates as [41]:

$$R = \sum_{i=1}^{n_d} \left[\frac{\partial F_i}{\partial X_i} - \sum_{j=1}^{n_d} \frac{\partial}{\partial X_i} \left(K_{ij} \frac{\partial G}{\partial X_j} \right) \right] - S \qquad (20)$$

and convergence is attained when

$$\xi \leq \xi_{\text{verge}} \; \forall \text{ inner nodes}, \qquad (21)$$

with ξ a convergence criterion based on the maximum between the discretized continuity and energy residuals [41]:

$$\xi \equiv \max \left(\frac{|R_{\Delta}^{\text{continuity}}|}{J^{-1}\rho}, \frac{|R_{\Delta}^{\text{energy}}|}{J^{-1}\rho E} \right). \qquad (22)$$

The user-defined convergence threshold ξ_{verge} is set to a value at least four orders of magnitude below the initial value of ξ for all the numerical simulations mentioned herein.

The WARP code has been validated with experimental results from Morris [51] and Lehr [33] that feature shock-induced combustion and detonation phenomena. For a detailed explanation of these validation cases, see Fusina [26]. WARP was shown to be capable of reproducing these experimental results with a sufficient degree of accuracy provided the spatial resolution was adequate. For example, in Lehr's blunt-body experiments where a projectile was fired in a quiescent hydrogen-air mixture at a sub-detonative speed, a simulation with WARP was able to reproduce the resulting frequency of the oscillating shock-combustion front to within 6%; and, for the steady case where the projectile is fired at a super-detonative speed, the position of the combustion front at the trailing edge of the projectile was captured to within 2% with the finest grid used (Figure 5).

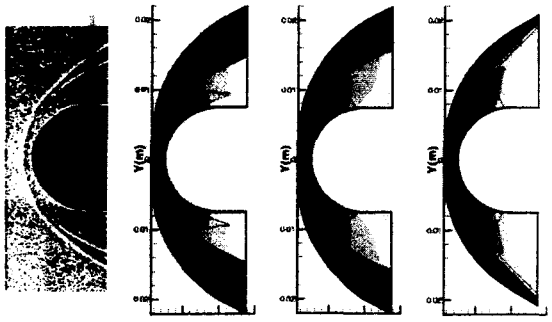

Fig. 5: Left: shadowgraph photography of Lehr's blunt body experiment for the super-detonative case. Right: overlaid temperature contours (flood: 15 levels between 450 K and 3400 K) and water contours (lines: 15 levels between 0.01 and 0.21) from numerical results from WARP using three different grid resolutions: (400×600), (200×300), (60×90).

Problem Setup

The combustor inlet conditions chosen correspond approximately to those that a shcramjet flying at Mach 12 and at an altitude 36,000 m would produce in its combustor: *i.e.* $M = 7$, $P = 23$ kPa, and $T = 750$ K. The hydrogen-air mixture was assumed to be fully premixed in stoichiometric proportions. Laminar flow was assumed with a constant temperature wall at 750 K. The Jachimowski model was used for the hydrogen-air combustion reactions. The flame-holder wedge angle was chosen such that it would create an $\sim 3^o$ overdriven ODW [26]: *i.e.* the angle was set to 13^o.

As stated above, only one section of the combustor is studied, the section corresponding to half of length D in Figure 4: this was taken to be the height of the computational domain which shall henceforth be termed

Table 3: Domain size and grid size for each quarter-section.

D/2 [m]	Domain Size (x[m],y[m])	Grid Size
0.07	(0.45,0.07)	(725×220)
0.085	(0.45,0.085)	(725×242)
0.1	(0.6,0.1)	(950×264)
0.115	(0.65,0.115)	(1025×284)

"quarter-section". Four different quarter-section heights were considered: 0.07 *m*, 0.085 *m*, 0.1 *m*, and 0.115 *m*. These values were chosen by considering the overall design of an external compression shcramjet (see Figure 1) flying at the conditions stated above. Using analytical oblique shock relations from gasdynamics, and assuming an inlet length of 15 *m*, the height of the combustor can be shown to be ~0.35 *m*, meaning that four quarter-sections of height 0.07 *m* to 0.085 *m* could be placed in such a combustor: the former would represent a minimum spacing and the latter a maximum. Similarly, for a slightly longer 20 *m* external compression shcramjet inlet, the combustor height can be shown to be ~0.47 *m*, meaning that four quarter-sections of height 0.1 *m* to 0.115 *m* could be placed in such a combustor.

Figure 6 shows the computational domain and grid used for the D/2 = 0.085 *m* case. This geometry produces quite a complex flowfield with many wave interactions occur; a detailed flowfield analysis will be given below. A different domain size was needed for each case in order to capture between 10 and 20 *cm* of the flowfield downstream of the point where the "ODW-reflection shock" (see Figure 11) intersects the lower symmetry plane. Table 3 gives the size of the domain and of the grid for each of the cases. The accuracy of the grid chosen will be assessed below.

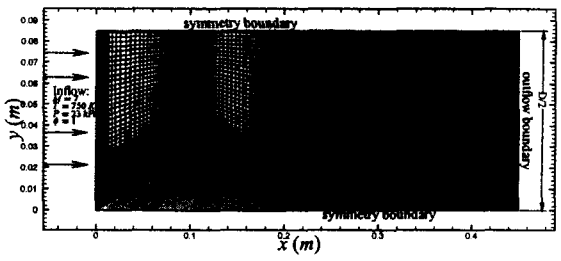

Fig. 6: Computational domain and grid used for D/2 = 0.085 *m* case. (Every third grid point shown for clarity).

Performance Parameters

Thrust Potential. The thrust potential at an engine section can be defined as the amount of thrust that an engine *would* produce if the flowfield at the particular section of interest were reversibly expanded to an outlet area equal to the inlet area: this is done by taking the difference in momentum between the outlet (found from the reversible expansion) and the inlet. The result is divided by the air mass flow rate [41, 52]:

$$\text{thrust potential}|_x \equiv \frac{\int_o (\rho u^2 + P)\, dA}{\dot{m}_{air}} - \frac{\int_i (\rho u^2 + P)\, dA}{\dot{m}_{air}}, \tag{23}$$

where $\dot{m}_{air}$ refers to the air mass flow rate in the engine, A refers to area, the subscript o refers to the engine outlet, the subscript i refers to the engine inlet and the subscript x refers to the station at which the thrust potential is to be evaluated. The outlet area is assumed to be equal to the inlet area, which is a valid assumption for shcramjet flows since they are typically underexpanded [1, 41].

In order to minimize the error from a flow expansion to constant pressure *or* constant area, Parent [41] devised a procedure to expand the flow to an iteratively determined backpressure, equal for all the streamlines. This pressure corresponds to the condition that the area of the expanded flow is equal to the outlet area. The procedure is briefly summarized below. First, an estimate for the desired outlet pressure, P_o, is made so that the velocity magnitude at the outlet, q_o, (reversibly expanded from each point at x), is found by numerically differentiating:

$$\frac{dq}{dP} = -\frac{RT}{Pq} \tag{24}$$

from q_x and P_x until P_o is reached. This yields T_o, ρ_o and q_o for each streamline. The total area at the outlet is to be equal to the inlet area, therefore the function:

$$f(P_o) = A_o(P_o) - A_i = \int_x \frac{1}{\rho_o q_o} d\dot{m} - A_i \tag{25}$$

must be minimized to find P_o (A_i is the inlet area and A_o is the outlet area). Then, each point at x is expanded again by Equation (24) to the proper outlet pressure so that the thrust potential at x, $F_P|_x$, is equal to [41]:

$$F_P|_x = \frac{\int_x \frac{\rho_o q_o^2 + P_o}{\rho_o q_o} d\dot{m}}{\dot{m}_{air}} - F_{P_{ref}} \tag{26}$$

with the two terms in Equation (26) relating to the two terms in Equation (23). In the calculation of thrust potential for the flowfields in this study, A_i is taken as the fraction of an external compression shcramjet inlet height corresponding to the fraction that a quarter-section would occupy in the combustor:

$$A_i = \frac{\text{D/2}}{\text{H}_{\text{combustor}}} \text{H}_{\text{inlet}} \tag{27}$$

where $\text{H}_{\text{combustor}}$ and H_{inlet} are the combustor and inlet heights of an external compression shcramjet flying at an altitude of 36,000 *m* and a Mach number of 12. They are calculated using analytical oblique shock relations from gasdynamics. For the D/2 = 0.07 *m* and

D/2 = 0.085 m cases, a 15 m inlet is assumed; and for the D/2 = 0.1 m and D/2 = 0.115 m cases, a 20 m inlet is assumed. Finally, in most of the subsequent discussion, "additive" thrust potential will be considered: this means that only the increase of F_P through the computational domain is calculated.

Drag Calculation. The streamwise component of the drag of the flameholder due to pressure can be expressed as the sum over all the nodes on the flameholder surface of the negative of the convective momentum flux at a node on the wall of the wedge [41]:

$$D_{p_x} = \sum_{i=1}^{sn} \Delta X_i [-F_1] \tag{28}$$

where "sn" refers to surface nodes and ΔX_i is the spacing between the boundary node and the closest inner node in curvilinear co-ordinates – it is either equal to $+1$ or -1 depending on the surface orientation. F_1 is defined above in Equation (2). The streamwise component of the drag of the flameholder due to viscous shear can be expressed as the sum over all the nodes on the flameholder surface of the negative of the viscous momentum flux at a node on the wall of the wedge [41]:

$$D_{f_x} = \sum_{i=1}^{sn} \Delta X_i \left[\sum_{j=1}^{2} K_{ns+1,j} \frac{\partial G}{\partial X_j} \right]. \tag{29}$$

$K_{ns+1,j}$ and G are defined above in Equation (6) and (2) respectively.

Heat Addition Calculation. It is important to quantify the amount of chemical energy released by the ODW. This is quite difficult due to the coupling between chemical and gasdynamic processes in an ODW [5]. In the propulsion industry, this difficulty is usually resolved by assuming a fictitious process where combustion takes place at constant pressure [45, 1, 5]. The heat released, or heat of reaction of the fuel, is then defined as the heat that must be removed from the combustion products to return to the temperature of the reactants [5]. This property is calculated at a standard reference state of 298 K and 1 atm as [1]:

$$Q_R = \sum_{k=1}^{ns} \frac{c_k}{m_k} \Delta H_{f,k} \tag{30}$$

where Q_R is the heat released and $\Delta H_{f,k}$ is the heat of formation of species k. This property was mass-flux averaged at each section of the combustor.

Grid Convergence Study

The case chosen for the grid convergence study was the one corresponding to a domain height of D/2 = 0.085 m. The grids for the other cases have the same grid density as this case but the number of nodes vary according to the domain size as shown in Table 3. Two more grid levels were chosen to assess the accuracy of the (725×242) grid: (483×161) and (1088×363). Figures 7 and 8 show the variation of additive thrust potential and mass-flux averaged heat released at each x-station of the domain. There is very little difference between the three grid levels. The points of maximum heat release and thrust potential, which are of particular interest here since they will affect the overall design of the combustor, are seen to be virtually identical in the three grids. Table 4 lists the values of drag and induction distance for the three grid levels – again there is very little difference between the three, except for the difference in the induction distance for the coarsest grid. Figure 9 shows the variation of temperature and density along the top and bottom boundaries of the domain. Along the top, there is very little

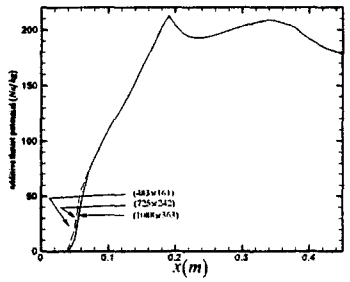

Fig. 7: Additive thrust potential along streamwise direction for the three different grid levels

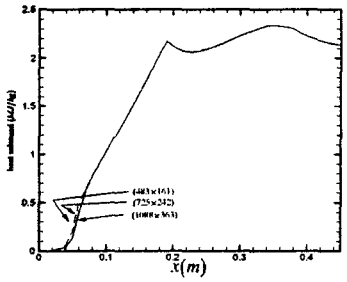

Fig. 8: Mass-flux averaged heat released along streamwise direction for the three different grid levels

Table 4: Summary of results for grid convergence study.

grid	$D_{p_x}[N]$	$D_{f_x}[N]$	χ_D [mm]
(1088×363)	3691	228	11.00
(725×242)	3684 (0.2)	230 (0.9)	10.78 (2.0)
(483×161)	3666 (0.6)	234 (3.5)	9.82 (11)

χ_D is determined by locating the position in the x-direction where the water mass fraction reaches 1% outside the boundary layer. Values in parentheses are percentages that show the percentage difference compared to the finest grid.

difference in the properties shown between the three grids. The bottom boundary, however, shows some differences in the range between $x = 0$ m and $x = 0.05$ m, and between $x = 0.20$ m and $x = 0.3$ m. The difference between the (483×161) and the (1088×363) grid exceeds 10% at several points while the difference between the (725×242) grid and the (1088×363) grid is contained to within 7% at points of maximum discrepancy. For the majority of points, however, the difference is less than 1%. Figure 10 shows the temperature profile at the $x = 0.2$ m section corresponding to the trailing edge of the flameholder. The coarse grid is quite inaccurate, especially within the boundary layer region. The (725×242) grid exhibits a much smaller difference compared to the finest grid, which does not exceed 7% at points of greatest discrepancy.

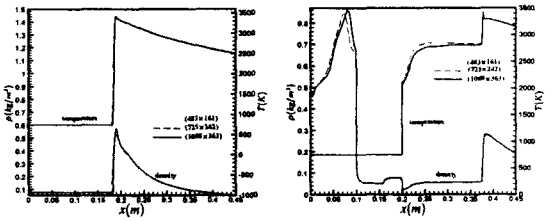

Fig. 9: Left: temperature and density along top symmetry boundary. Right: temperature and density along bottom surface and symmetry boundary.

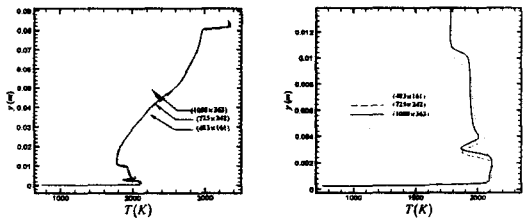

Fig. 10: Left: temperature profile at trailing edge of the flame holder. Right: boundary layer detail of temperature profile.

The (725×242) grid level was the one selected as it has been deemed to be sufficiently accurate in determining the parameters of interest for the purposes of this investigation (*i.e.* thrust potential, heat released and drag) and in predicting flowfield variable quantities.

Discussion of Results

General Flowfield Analysis

Figure 11 shows temperature contours depicting the flowfields of all four cases. It can be seen that they exhibit very similar flowfield characteristics with complex wave interactions, labelled in Figure 11 and identified as follows: (1) the ODW which begins at the $x = 0.05$ m section; (2) the reflection of the ODW from the top symmetry boundary in the form of a shock, termed "ODW-reflection shock"; (3) the rarefaction wave centred at the top of the flameholder, at $x = 0.1$ m; (4) the shock emanating from the trailing edge of the wedge; (5) the expansion region downstream of the ODW-reflection shock. Further, when the ODW-reflection shock and the trailing edge shock intersect, they form two transmitted shocks: (6) the transmitted trailing edge shock; and (7) the transmitted ODW-reflection shock. Also observed is: (8) a shock which is the reflection of (7) on the bottom symmetry boundary. The transmitted trailing edge shock – *i.e.* (6) – and (8) intersect, resulting in (9), a single resultant shock only captured for the D/2 = 0.07 m case. Expansion regions in addition to (5) are also observed in between each shock which are labelled R1, R2, and R3 in Figure 11. These occur as a consequence of the intersecting shocks. A small recirculation region which forms at the trailing edge of the wedge is also observed. It starts at $x \simeq 0.175$ m and ends at $x \simeq 0.225$ m. A very weak shock is formed due to the adverse pressure gradient of the recirculation at $x \simeq 0.175$ m. All the shocks formed due to the interaction of the ODW-reflection shock – *i.e.* (2) – with the bottom boundary, as well as (2) itself and the trailing edge shock, are reactive shocks, but not heat releasing waves. The temperatures are high enough for dissociation to occur through them as the atomic oxygen mass fraction increases, and the water mass fraction decreases. Conversely, in the expansion regions, as the pressure and temperature drops, recombination occurs and the opposite trend in species production is observed.

Figures 12 to 15 show the variation of additive thrust potential, mass-flux averaged heat released, temperature and pressure as well as the variation of mass-flux averaged mass fractions for H_2O, OH, H and O for the D/2 = 0.085 m case. Both F_P and Q_R exhibit two local maxima and one local minimum. The first maximum occurs at the section where the ODW intersects the top symmetry boundary. The local minimum occurs at a section a few centimeters downstream of the trailing edge of the wedge. The second maximum occurs at a section near the intersection of the ODW-reflection shock and the trailing edge shock. The first three dashed lines in these figures correspond to these three sections. The fourth dashed line is drawn for reference as the section where the transmitted ODW-reflection shock – *i.e.* (7) – reflects on the bottom symmetry boundary. The trend in Q_R and F_P is identical since the thrust potential of the flow is expected to increase as heat is added to the flow. Note that the value of Q_R at the second maximum is slightly greater than the value at the first maximum; while for F_P, the second maximum value is approximately equal to the first. This result can be explained by examining the behaviour of the other mass-flux averaged values for this

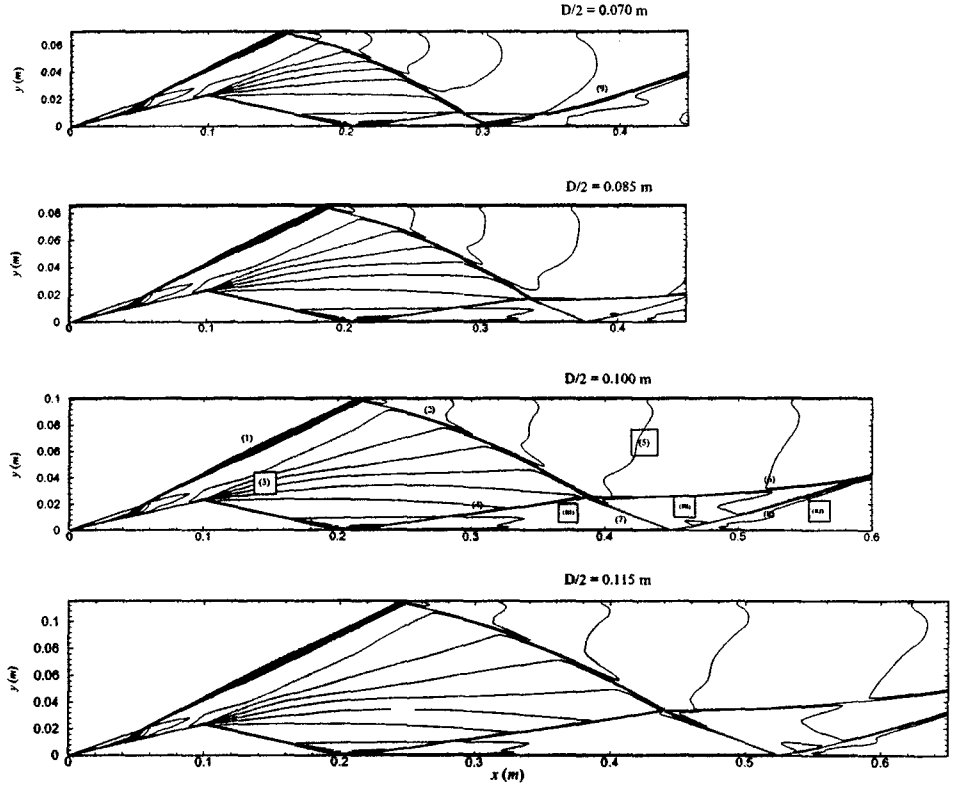

Fig. 11: Temperature contours for the different cases. (Fifteen contour levels between 700 K and 3500 K are shown).

case. The averaged temperature, water, hydrogen and oxygen mass fraction vary little after the ODW intersects the top boundary. However, the atomic oxygen and atomic hydrogen mass fractions – which represent dissociation reactions – vary significantly: after reaching a maximum at the same point where Q_R and F_P are at a local minimum, they decrease, and in this same region, Q_R and F_P increase again, together with the water mass fraction, albeit only slightly. Also note the drastic averaged pressure drop (due to the expansion regions) where Q_R and F_P increase. The values of c_O and c_H at their minimum (at the section where (2) and (4) intersect) are lower than those at the section where the ODW intersects the top boundary; the opposite (albeit less drastic) trend is observed for c_{H_2O} values: this explains the higher value of Q_R at its second maximum. The value of F_P does not reach the same value at its second maximum, since the pressure at that section is much lower than at the section where the first maximum occurs, *i.e.* some expansion has already taken place.

The same pattern in Q_R and F_P is found in the other cases (D/2 = 0.07 m, D/2 = 0.1 m and D/2 = 0.115 m) as Figures 16 and 17 show. Of note is the large drop in thrust potential in the D/2 = 0.07 m case, as the flow passes through the final resultant shock (9).

Table 5 quotes the values of Q_R and F_P at the two maximum locations together with the values of drag

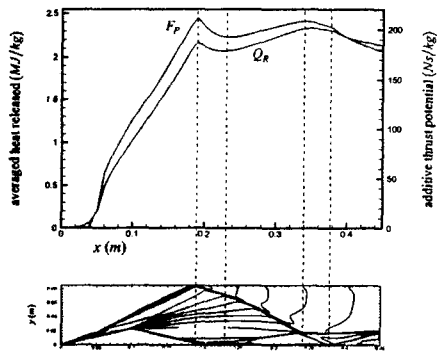

Fig. 12: Additive thrust potential and averaged heat released through the combustor for the D/2 = 0.085 m case with a temperature field (15 contour levels between 750 K and 3500 K) shown for reference.

on the wedge surface. As can be seen, both Q_R and F_P attain higher values as D/2 increases within the range of 0.07 m to 0.085 m, and from 0.1 m to 0.115 m.

From this analysis the best position to start the nozzle would be where the second maximum of F_P occurs which is well before the section where ODW-reflection shock meets the bottom boundary (x=0.34 m for the D/2=0.085 m case): in this way, most of the thrust po-

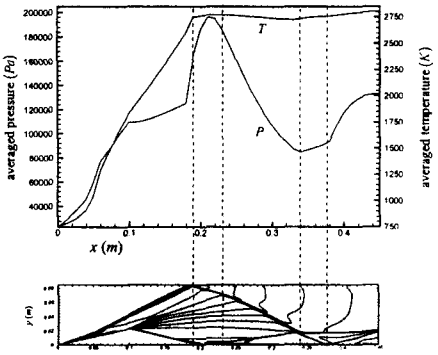

Fig. 13: Mass-flux averaged pressure and temperature through the combustor for the D/2 = 0.085 *m* case with a temperature field (15 contour levels between 750 *K* and 3500 *K*) shown for reference.

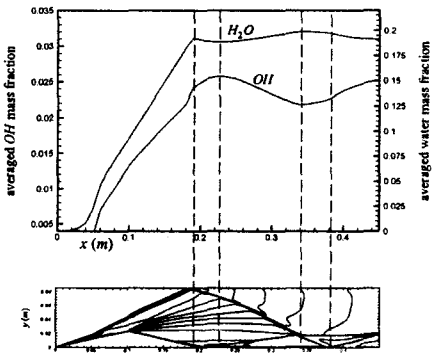

Fig. 14: Mass-flux averaged *OH* and O_2 mass fraction through the combustor for the D/2 = 0.085 *m* case with a temperature field (15 contour levels between 750 *K* and 3500 *K*) shown for reference.

tential could be realized and the possible recirculation region due to a possible shock-boundary layer interaction (assuming the presence of a wall in a complete combustor configuration – see Figure 4) could still be avoided. The drag does not change at all for the four different cases and the drag due to viscous shear is only 6% of the pressure drag. This means that the flame holders will not hamper the shcramjet's performance because of their skin friction drag, and, as the thrust potential trends imply, the pressure drag and wave drag is completely overshadowed by the heat addition due to combustion.

Combustor Performance

The question remains whether the performance of a shcramjet with the present combustor design is comparable to that of a shcramjet with the original shcramjet combustor design (see Figure 4). This question is

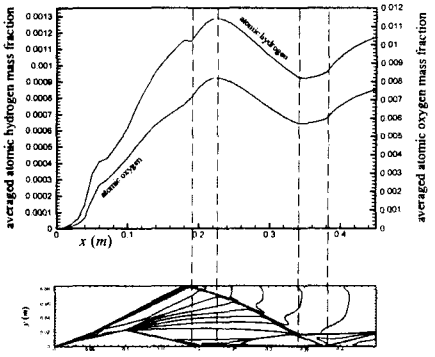

Fig. 15: Mass-flux averaged *H* and *O* mass fraction through the combustor for the D/2 = 0.085 *m* case with a temperature field (15 contour levels between 750 *K* and 3500 *K*) shown for reference.

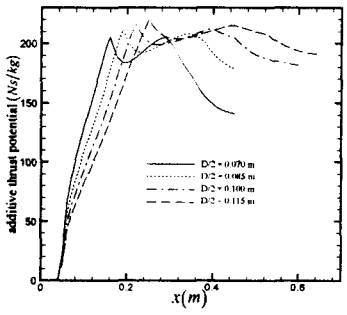

Fig. 16: Additive thrust potential along streamwise direction for the different cases.

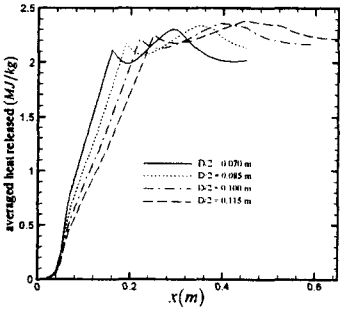

Fig. 17: Mass-flux averaged heat released along streamwise direction for the different cases.

answered by introducing a "fuel-specific impulse potential", based on the thrust potential. It can be defined as:

$$I_{sp_P} = \frac{\left(F_P - F_{P_{ref}}\right)\dot{m}_{air}}{\dot{m}_{fuel} g} \qquad (31)$$

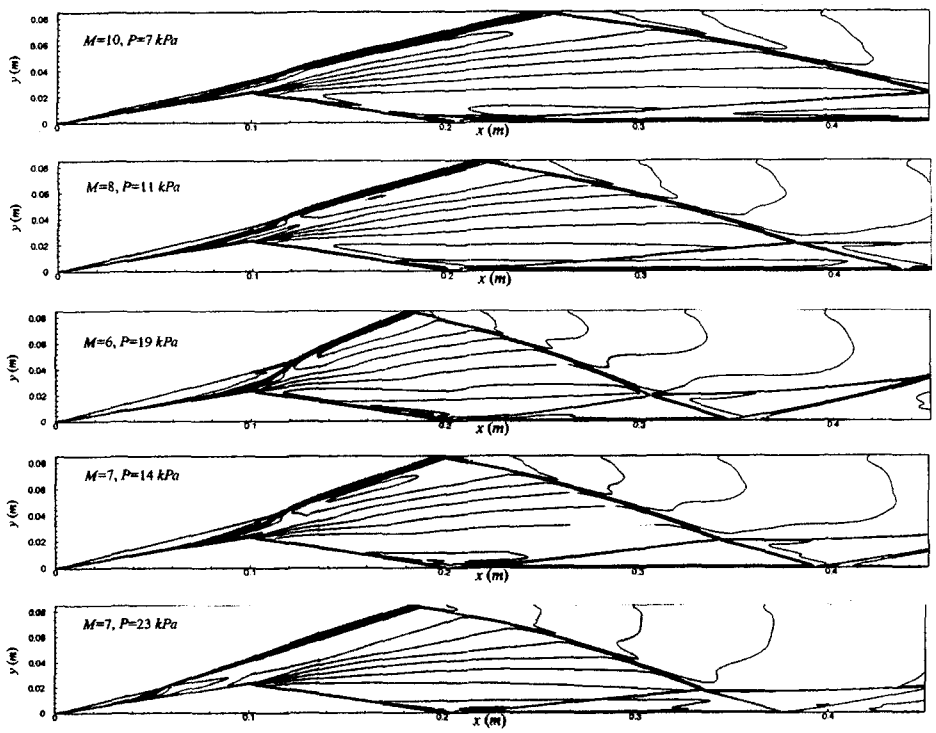

Fig. 18: Temperature contours for the different cases. (Fifteen contour levels between 700 K and 3500 K are shown).

Table 5: Drag values and peak values for thrust potential and mass flux averaged heat released for each case.

D/2 [m]	F_{P_1} [Ns/kg]	F_{P_2} [Ns/kg]	Q_{R_1} [MJ/kg]	Q_{R_2} [MJ/kg]
0.070	205	205	2.12	2.32
0.085	211	211	2.17	2.33
0.100	216	212	2.22	2.36
0.115	219	215	2.25	2.38

The subscripts 1 and 2 represent the first and second peak value respectively.

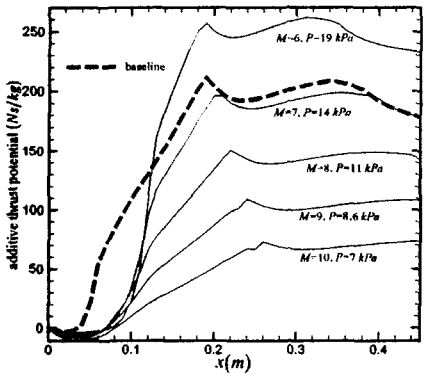

Fig. 19: Left: additive thrust potential along streamwise direction for some off-design cases.

where g is the gravitational acceleration, $\dot{m}_{fuel}$ is the fuel mass flow rate through the engine and $\dot{m}_{air}$ is the air mass flow rate through the engine. The fuel-specific impulse is a means of comparing different hypersonic engines since it is practically independent of the vehicle's dimensions. Since the calculation is based on thrust potential which assumes a perfect expansion, the value of a fuel-specific impulse potential will be higher than an actual value of fuel-specific impulse, based on a real nozzle expansion. In Equation (31), F_P is taken as the thrust potential evaluated at the $x = 0.34$ m section of the D/2 = 0.085 m case (*i.e.* where the second maximum occurs); $F_{P_{ref}}$ is taken as the thrust potential evaluated at the inlet of a shcramjet flying at a Mach number of 12 at 36,000 m altitude, assuming a stoichiometric hydrogen-air mixture.

The value for I_{sp_p} obtained is 1460 s. Dudebout [5] obtained a value of approximately 1000 s for I_{sp} for a Mach 12 shcramjet at 36,000 m employing the original combustor design and the assumption of inviscid flow. The value obtained in this calculation is significantly higher due to the ideal expansion in the thrust potential calculation and gives sufficient reason for this design to be studied further. Had this value been lower than Dudebout's, then this combustor design concept would not have been worth considering. The "additive" value for I_{sp_p} in the combustor section alone is 728 s. Note that typical values for I_{sp} for a scramjet flying at Mach 12 are in the vicinity of 1200 s, and for a rocket, ~500 s [5, 1].

Off-Design Cases

More numerical simulations were conducted to determine the effect of off-design conditions on the combustor's thrust potential. The combustor inflow Mach number and pressure were varied in order to simulate off-design conditions. The D/2=0.085 m case with inflow conditions of $M = 7$, $P = 23$ kPa, and $T = 750$ K was taken as a "baseline" case. The additive thrust potential variation for the baseline case and off-design cases are shown in Figure 19. Figure 18 shows temperature contours for the off-design cases and the baseline case. First, note the difference between the M=7, P=23 kPa case and the M=7, P=14 kPa case. The temperature contours show that the induction distance for the lower pressure case increases, but the ODW angle does not change significantly and the other flow features are very similar: hence, as shown in Figure 19, there is little difference between the variation of thrust potential within the combustor for these two cases.

For the cases where pressure is further lowered, and the Mach number is increased to 8 and 10, Figure 19 shows that the combustor's performance degrades as the Mach number increases. A higher Mach number over the wedge causes a shallower shock and a shallower ODW: the capture area in this case is too large to realize a sufficient thrust potential for the combustor at these high Mach numbers.

It was not possible to achieve a converged solution below a Mach number of 6: the rarefaction wave emanating from the top of the wedge surface would interact with the deflagration waves before the ODW would fully form; hence we speculate that this gives rise to an unsteady flowfield with unsteady shock-combustion fronts. The M=6, 19 kPa case shows a longer induction region than the M=7, 14 kPa case and hence a larger shock-induced combustion region. The ODW angle is also observed to be slightly steeper. It has been observed via numerical simulations [26, 5] that the heat release through the shock-induced combustion zone is higher than that through a fully-formed ODW. In this lower Mach number case, the shock-induced combustion zone is larger than in the higher Mach number cases which can explain the higher thrust potential. Further, since the ODW is steeper, the size of the capture area gives rise to a higher value of thrust potential for this case.

Finally, note, in Table 6 that the skin friction drag accounts for an increasing percentage of total drag as the Mach number increase; this is another factor that contributes to performance degradation at higher Mach numbers. Also shown in this table are the values for additive I_{sp_p} for the different cases (all evaluated at the x=0.34 m section). The difference between the additive I_{sp_p} for the Mach 7 case and the Mach 8 case is 25% which means that employing this shcramjet combustor design above this Mach number would no longer be viable, since the specific impulse potential would drop below that of the shcramjet with the original combustor design.

Table 6: Drag values and peak values for thrust potential and mass flux averaged heat released for each case.

Mach	P [kPa]	additive I_{sp_p} [s]	D_p, N	D_f, N
7	23	720	3684	230 (6)
7	14	700	1900	170 (8)
6	19	920	1929	155 (7)
8	11	520	1850	210 (10)
10	7	256	1700	250 (13)

The values in parentheses are the percentages of the friction drag to the total drag.
Additive I_{sp_p} values are calculated at the x=0.34 m section for all cases.

Conclusions

The proposed shcramjet combustor design based on wedge-shaped flame-holders has been demonstrated to be a viable alternative to the original shcramjet combustor design between combustor inlet Mach numbers of 6 and 8 and combustor inlet pressures between 11 kPa and 23 kPa – assuming a shcramjet flight Mach number of 12 and an altitude of 36,000 m. The combustor flowfield is quite complex with many shock-expansion wave interactions, but thrust potential and fuel-specific impulse potential calculations have shown that, between the above limits, the energy addition to the shcramjet flow would be sufficient to obtain a comparable value for fuel-specific impulse as other hypersonic airbreathing propulsion vehicles. The skin friction drag of the wedges has been shown to be minimal (within the operational Mach number range) and will therefore not hamper the shcramjet's performance. Operation of this combustor at different shcramjet flight Mach numbers would require a variable geometry.

Future studies should be conducted to further assess the viability of this design: first, wall effects must be considered, as well as the effects of incomplete mixing. A two-dimensional CFD simulation of an entire shcramjet flowfield with this combustor should also be undertaken.

References

1) Pratt, D. T. and Heiser, W. H., *Hypersonic Airbreathing Propulsion*, AIAA Education Series, 1994.

2) McClinton, C. R., Raush, D. R., Sitz, J., and Reukauf, P., "Hyper-X Program Status," *AIAA Paper 2001-1910*, April 2001, presented at the 10th AIAA International Aerospace Planes Hypersonics Technologies Conference, Kyoto, Japan.

3) Bouchez, M., N., M., LeBoucher, C., and Souchet, M., "Scramjet Combustor Design in France," *AIAA Paper 95-6094*, 1995.

4) Kobayashi, S. and M., M., "Japanese Spaceplane Program Overview," *AIAA Paper 95-6002*, 1995.

5) Dudebout, R., *Numerical Simulation of Hypersonic Shock-Induced Combustion Ramjet Flowfields*, Ph.D. thesis, University of Toronto, Toronto, ON, Canada, 1995, Graduate Department of Aerospace Science and Engineering.

6) Sislian, J. P., "Detonation Wave Ramjets," *Scramjet Propulsion*, edited by E. T. Curran and S. N. B. Murthy, Vol. 189 of *Progress in Aeronautics and Astronautics*, chap. 13, American Institute of Aeronautics and Astronautics, Inc., Washington, DC, 2001, pp. 823–889.

7) Jones, J. S., Bangert, L. S., Garber, D. P., Huebner, L. D., McKinley Jr., R. E., Sutton, K., Swanson Jr., R. C., and Weinstein, L., "Research Opportunities in Advanced Aerospace Concepts," TM 210547, NASA, 2000.

8) Cambier, J., Adelman, H., and Menees, G., "Numerical Simulation of an Oblique Detonation Wave Engine," *AIAA Paper 88-0063*, 1988.

9) Oswatitsch, K., "Pressure Recovery for Missiles with Reaction Propulsion at High Supersonic Speeds. (The Efficiency of Shock Diffusers)," TM 1140, NASA, 1947.

10) Roy, M. M., "Moteurs thermiques," *Comptes Rendus de l'Académie des Sciences*, Vol. 222, 1946.

11) Dunlap, R., Brehm, R. L., and Nicholls, J., "A Preliminary Study of the Application of Steady-State Detonation Combustion to a Reaction Engine," *Journal of Jet Propulsion*, Vol. 28, No. 6, 1958, pp. 451–456.

12) Sargeant, W. H. and Gross, R. A., "A Detonation Wave Hypersonic Ramjet," Tech. Rep. 589, AFOSR, 1959.

13) Townend, L. H., "Detonation Ramjets for Hypersonic Aircraft," *Royal Aircraft Establishment Technical Report 70218*, 1970.

14) Morrison, R. B., "Evaluation of the Oblique Detonation Wave Ramjet," CR 145358, NASA, 1978.

15) Morrison, R. B., "Oblique Detonation Wave Ramjet," CR 159192, NASA, 1980.

16) Ostrander, M., Hyde, J., Young, M., and Kissinger, R., "Standing Oblique Detonation Wave Engine Performance," *AIAA Paper 87-2002*, 1987.

17) O'Brien, C. and Kobayashi, A., "Advanced Earth-to-Orbit Propulsion Concepts," *AIAA Paper 86-1386*, 1986.

18) Menees, G., Adelman, H., Cambier, J., and Bowles, J., "Wave Combustors for Trans-Atmospheric Vehicles," *9th International Symposium on Airbreathing Engines*, 1989.

19) Sheng, Y. and Sislian, J. P., "A Model of a Hypersonic Two-Dimensional Oblique Detonation Wave Ramjet," Tech. Rep. 257, UTIAS, 1985.

20) Dudebout, R., Sislian, J. P., and Oppitz, R., "Numerical Simulation of Hypersonic Shock-Induced Combustion Ramjets," *Journal of Propulsion and Power*, Vol. 14, No. 6, 1998, pp. 869–879.

21) Sislian, J. P., Dudebout, R., Schumacher, J., Islam, M., and Redford, T., "Incomplete Mixing and Off-Design Effects on Shock-Induced Combustion Ramjet Performance," *Journal of Propulsion and Power*, Vol. 16, No. 1, 2000, pp. 41–48.

22) Sislian, J. P., Schirmer, H., Dudebout, R., and Schumacher, J., "Propulsive Performance of Hypersonic Oblique Detonation Wave and Shock-Induced Combustion Ramjets," *Journal of Propulsion and Power*, Vol. 17, No. 3, 2001, pp. 599–604.

23) Schumacher, J., *Effects of Incomplete Fuel-Air Mixing on the Performance Characteristics of Hypersonic Shock-Induced Combustion Ramjets (Shcramjets)*, Master's thesis, University of Toronto, Toronto, ON, Canada, 1995, Graduate Department of Aerospace Science and Engineering.

24) Sislian, J. P. and Schumacher, J., "A Comparative Study of Hypersonic Fuel/Air Mixing Enhancement by Ramp and Cantilevered Ramp Injectors," *AIAA 99-4873*, Nov. 1999, presented at the 9th AIAA International Aerospace Planes Hypersonics Technologies Conference, Norfolk, VA.

25) Parent, B., Sislian, J. P., and Schumacher, J., "Numerical Investigation of the Turbulent Mixing Performance of a Cantilevered Ramp Injector," *AIAA Journal*, Vol. 40, No. 8, 2002, pp. 1559–1566.

26) Fusina, G., *Numerical Investigation of Oblique Detonation Waves for a Shcramjet Combustor*, Ph.D. thesis, University of Toronto, Toronto, ON, Canada, 2003, Graduate Department of Aerospace Science and Engineering.

27) Fusina, G., Sislian, J. P., and Parent, B., "Computational Study of Formation and Stability of Standing Oblique Detonation Waves," *AIAA Paper 2004-1125*, 2004, presented at the AIAA 42nd Aerospace Sciences Meeting and Exhibit, Jan 5–8, 2004, Reno, Nevada.

28) Nettleton, M., *Gaseous Detonations: their Nature and Control*, Chapman and Hall Ltd., 1987.

29) Lee, J., "Initiation of Gaseous Detonation," *Annual Review of Phys. Chem.*, Vol. 28, No. 75, 1977.

30) Li, C., Kailasanath, K., and Oran, E., "Detonation Structures behind Oblique Shocks," *Physics of Fluids*, Vol. 6, No. 4, 1994, pp. 1600–1611.

31) Kailasanath, K., Oran, E., Boris, J., and Young, T., "Determination of Detonation Cell Size and the Role of Transverse Waves in Two-Dimensional Detonations," *Combustion and Flame*, Vol. 61, 1985, pp. 199–209.

32) Shepherd, J., Moen, I., Murray, S., and Thibault, P., "Analyses of the Cellular Structure of Detonations," *21st International Symposium on Combustion*, 1988, pp. 1649–1658.

33) Lehr, H. F., "Experiments in Shock-Induced Combustion," *Astronautica Acta*, Vol. 17, 1972, pp. 589–597.

34) Choi, J. Y., Jeung, I. S., and Yoon, Y., "Computational Fluid Dynamics Algorithms for Unsteady Shock-Induced Combustion, Part 1: Validation," *AIAA Journal*, Vol. 38, No. 7, 2000, pp. 1179–1187.

35) Matsuo, A., Fujii, K., and Fujiwara, T., "Flow Features of Shock-Induced Combustion Around Projectile Travelling at Hypervelocities," *AIAA Journal*, Vol. 33, No. 6, 1995, pp. 1056–1062.

36) Wilson, G. J. and Sussman, M. A., "Computation of Unsteady Shock-Induced Combustion Using Logarithmic Species Conservation Equations," *AIAA Journal*, Vol. 31, No. 2, 1993, pp. 294–301.

37) Viguier, C., Figueira da Silva, L., Desbordes, D., and Deshaies, B., "Onset of Oblique Detonation Waves: Comparison between Experimental and Numerical Results for Hydrogen-Air Mixtures," *26th International Symposium on Combustion, The Combustion Institute, Pittsburgh, PA*, 1997, pp. 3023–3031.

38) Islam, M., *Off-Design Performance of Oblique Detonation Wave Ramjets*, Master's thesis, University of Toronto, Toronto, ON, Canada, 1996, Graduate Department of Aerospace Science and Engineering.

39) Viviand, H., "Conservative Forms of Gas Dynamics Equations," *La Recherche Aérospatiale*, , No. 1, Jan. 1974, pp. 65–68.

40) Vinokur, M., "Conservative Equations of Gas-Dynamics in Curvilinear Coordinate Systems," *Journal of Computational Physics*, Vol. 14, 1974, pp. 105–125.

41) Parent, B., *Computational Study of Fuel Injection in a Shcramjet Inlet*, Ph.D. thesis, University of Toronto, Toronto, ON, Canada, 2002, Graduate Department of Aerospace Science and Engineering.

42) McBride, B. J. and Reno, M. A., "Coefficients for Calculating Thermodynamic and Transport Properties of Individual Species," TM 4513, NASA, Oct. 1993.

43) Chase, M. W., "JANAF Thermochemical Tables, 3rd. Ed. parts I and II," *Journal of Physical and Chemical Reference Data*, Vol. 14, 1985, Suppl. 1.

44) Dixon-Lewis, G., "Computer Modelling of Combustor Reactions," *Combustion Chemistry*, edited by W. C. Gardiner, chap. 2, Springer Verlag, New-York, NY, 1984, pp. 21–125.

45) Anderson, J. D., *Hypersonic and High-Temperature Gas Dynamics*, McGraw-Hill, 1989.

46) Jachimowski, C. J., "An Analytical Study of the Hydrogen-Air Reaction Mechanism With Application To Scramjet Combustion," TP 2791, NASA, 1988.

47) Parent, B. and Sislian, J. P., "The Use of Domain Decomposition in Accelerating the Convergence of Quasihyperbolic Systems," *Journal of Computational Physics*, Vol. 179, No. 1, 2002, pp. 140–169.

48) Roe, P. L., "Approximate Riemann Solvers, Parameter Vectors, and Difference Schemes," *Journal of Computational Physics*, Vol. 43, 1981, pp. 357–372.

49) Yee, H. C. and Shinn, J. L., "Semi-Implicit and Fully Implicit Shock-Capturing Methods for Nonequilibrium Flows," *AIAA Journal*, Vol. 27, 1989, pp. 299–307.

50) Jenssen, C. B. and Weinerfelt, P. A., "Parallel Implicit Time-Accurate Navier-Stokes Computations Using Coarse Grid Correction," *AIAA Journal*, Vol. 36. No. 6, 1998, pp. 946–951.

51) Morris, C. I., Kamel, M. R., and Hanson, R. K., "Expansion Tube Investigation of Ram Accelerator Projectile Flowfields," *AIAA Paper 96-2680*, 1996.

52) Riggins, D. W., McClinton, C. R., and Vitt, P. H., "Thrust Losses in Hypersonic Engines Part 1: Methodology," *Journal of Propulsion and Power*, Vol. 13, No. 2. 1997, pp. 281–287.

Appendix: Nomenclature

Roman symbols

a	=	coefficient for thermochemical polynomial
$\mathscr{A}$	=	coefficient used to calculate k_f
c	=	mass fraction
C_P	=	specific heat at constant pressure
D	=	spacing between flameholders
D_{f_x}	=	drag due to viscous shear in x direction
D_{p_x}	=	drag due to pressure in x direction
e	=	internal energy
E	=	total energy
$\mathscr{E}$	=	coefficient used to calculate k_f
F	=	convection flux vector
F_P	=	thrust potential
$F_{P_{ref}}$	=	reference thrust potential
g	=	gravitational acceleration
G	=	vector of diffusion variables
h	=	enthalpy
H	=	shcramjet component height
I_{sp}	=	fuel-specific impulse
I_{sp_P}	=	fuel-specific impulse potential
J	=	metric Jacobian
k_b	=	backward reaction rate constant
k_f	=	forward reaction rate constant
K	=	diffusion matrix
K_c	=	equilibrium constant
m	=	molecular weight
$\dot{m}$	=	mass flow rate
M	=	Mach number
n	=	coefficient used to calculate k_f
n_s	=	number of species
n_d	=	number of dimensions
N_e	=	number of elementary reactions involving a species
N_l	=	number of species involved in an elementary reaction
P	=	pressure
Q	=	vector of conserved variables
Q_R	=	heat released due to chemical reactions
R	=	gas constant
$\mathscr{R}$	=	universal gas constant
s^o	=	entropy at reference state

S = vector of source terms
T = temperature
v = velocity vector
V = contravariant velocity vector
$\dot{W}$ = vector of species production terms
x = Cartesian coordinate
X = curvilinear coordinate
y = Cartesian coordinate

Greek symbols

δ = flow deflection angle
δ_{ij}^{Kr} = Kronecker delta
ε = detonation wave angle
η = third body efficiency
θ = flow angle
κ = thermal conductivity
μ = viscosity
ν = mass diffusion coefficient
ν' = stoichiometric coefficient for reactants
ν'' = stoichiometric coefficient for products
ξ = convergence criterion
ξ_{verge} = user-defined convergence criterion threshold
ρ = density
ϕ = equivalence ratio
χ = mole fraction
χ_D = induction distance outside boundary layer in the x-direction

Mixed Symbols

ΔG^o = difference in Gibbs free energy at reference state between products and reactants
ΔH_f = heat of formation
ΔX_i = spacing between boundary node and first inner node in curvilinear coordinates

Acronyms

CFD = *c*omputational *f*luid *d*ynamics
CFL = *C*ourant-*F*riedrichs-*L*ewy
CJ = *C*hapman-*J*ouguet
ODW = *o*blique *d*etonation *w*ave
WARP = *w*indow-*a*llocatable *r*esolver for *p*ropulsion